

Sparse-as-Possible SVBRDF Acquisition

Zhiming Zhou^{1,2} Guojun Chen² Yue Dong² David Wipf² Yong Yu¹ John Snyder² Xin Tong²

¹Shanghai Jiao Tong University ²Microsoft Research



Figure 1: SVBRDFs reconstructed by our method and relit. The Bear model (a) is recovered from a single image ($k=1$), while Mouse (b), Pig (c), and PaintSph (d) are reconstructed from multiple images ($k=36$, 54 , and 17 , respectively). The sparse blend solved for at each surface point combines a single representative ($n=1$) in the Bear, three ($n=3$) in Mouse, four ($n=4$) in Pig, and five ($n=5$) in PaintSph.

Abstract

We present a novel method for capturing real-world, spatially-varying surface reflectance from a small number of object views (k). Our key observation is that a specific target’s reflectance can be represented by a small number of custom basis materials (N) convexly blended by an even smaller number of non-zero weights at each point (n). Based on this *sparse basis/sparser blend* model, we develop an SVBRDF reconstruction algorithm that jointly solves for n , N , the basis BRDFs, and their spatial blend weights with an alternating iterative optimization, each step of which solves a linearly-constrained quadratic programming problem. We develop a numerical tool that lets us estimate the number of views required and analyze the effect of lighting and geometry on reconstruction quality. We validate our method with images rendered from synthetic BRDFs, and demonstrate convincing results on real objects of pre-scanned shape and lit by uncontrolled natural illumination, from very few or even a single input image.

Keywords: SVBRDF acquisition, Sparse reconstruction

Concepts: •Computing methodologies → Reflectance modeling;

1 Introduction

Realistic CG rendering must capture the rich and detailed reflectance of real-world materials. Surface reflectance is represented by the 6D spatially varying bidirectional reflectance distribution function (SVBRDF), describing radiance at each surface point x

Permission to make digital or hard copies of all or part of this work for personal or classroom use is granted without fee provided that copies are not made or distributed for profit or commercial advantage and that copies bear this notice and the full citation on the first page. Copyrights for components of this work owned by others than ACM must be honored. Abstracting with credit is permitted. To copy otherwise, or republish, to post on servers or to redistribute to lists, requires prior specific permission and/or a fee. Request permissions from permissions@acm.org. © 2016 ACM.

SA '16 Technical Papers., December 05-08, 2016, , Macao

ISBN: 978-1-4503-4514-9/16/12

DOI: <http://dx.doi.org/10.1145/2980179.2980247>

lit from direction i and reflected to view direction o . High dimensionality makes SVBRDF acquisition challenging; exploiting redundancy is crucial to make it efficient.

Two subproblems must be solved. First, we need a faithful yet compact SVBRDF model. Fewer degrees of freedom need less data to fit. Second, we need a robust method to identify points on the object sharing reflectance. To limit the number of measurements, the same material should appear at multiple points on the target, and its outgoing radiance observed in different directions or in response to different lighting. But such differences yield different measurements, making it hard to link points belonging to the same material.

Several methods directly link points by making simplistic assumptions about the spatial distribution of reflectance: that it is low-frequency [Zickler et al. 2005], or correlated to color [Goldman et al. 2010; Lombardi and Nishino 2012] or single-view response to ambient illumination [Aittala et al. 2015].

The *sparse basis* model reduces degrees of freedom by assuming surface reflectance blends over a limited number of target-specific basis materials. It links points implicitly by matching captured measurements to ones synthesized from this basis. The basis materials and their spatial blending weights can be jointly optimized [Chen et al. 2014], but a blending weight must be determined for *each* basis component per surface point. Since tens or hundreds of basis materials are needed in typical targets, many views are required for a good reconstruction.

To reduce the number of views, this blend can be further constrained as locally linear [Dong et al. 2010; Ren et al. 2011], over a very small set of “nearest neighbor” basis materials at each surface point. This *sparse blend* model in general yields a difficult, mixed discrete/continuous problem to simultaneously recover the basis as well as the neighborhood candidates and their blending weights. Previous methods instead acquire the BRDF basis in a separate manual phase [Dong et al. 2010] or using a reference chart [Ren et al. 2011], and then solve for the blending weights from another set of measurements. The BRDF basis must be chosen beforehand based on expert knowledge of the target. Furthermore, the optimal basis components to blend are not necessarily close in BRDF space.

We present a new method for acquiring SVBRDFs from very few input images which simultaneously exploits the sparse basis and

sparser blend priors, without manually specifying the basis or linking points via simple proxies. Specifically, we assume that reflectance can be modeled by a convex combination over a limited number of target-specific basis materials, called *representatives*, where the number of non-zero blending weights at each point is significantly smaller than the number of representatives. Our assumption is that reflectance variation in typical objects forms a patch-work – while the number of patch types is not known beforehand and might be fairly large, an individual patch blends between only a few basic materials.

Our approach minimizes relative reconstruction error of the captured measurements, and penalizes the number of representatives (N) and maximum number of them to blend at any point (n). By formulating representatives as a linear combination over a large, predefined set of *generic BRDFs*, the resulting constrained optimization problem can be solved iteratively via simple quadratic programming applied alternately to the representatives and the blending weights.

Our formulation also enables analysis of lighting and geometry optimality and the minimal number of views necessary for robust reconstruction. We find that natural lighting is better than directional, and curved objects better than flat ones. We validate our approach with images rendered from synthetic SVBRDFs and evaluate our system on real objects with known geometry, lit by passive environmental lighting. Our method successfully captures SVBRDFs from very few or even a single image.

2 Related Work

Independent reconstruction Surface reflectance can be reconstructed independently at each point, for example using a gonioreflectometer [McAllister 2002; Lawrence et al. 2006]. Gardner et al. [2003] fit a parametric model at each surface point from measurements acquired from scanning a linear light source. Aittala et al. [2013] estimate a two-lobe model for each surface point by capturing images lit by an LCD screen. Assuming that natural illumination contains sharp edges, Dong et al. [2014] reconstruct surface reflectance from a video of a rotating object, with known geometry under unknown environmental lighting. Independent reconstruction at each point ignores the redundancy of real world materials and requires many measurements.

Coherent reconstruction Reflectance sharing [Zickler et al. 2005] formulates SVBRDF reconstruction as a scattered interpolation problem, and fits both its angular and spatial distribution with basis functions. This trades off angular and spatial resolution and only works with smoothly varying materials. Assuming pixels with similar chromaticity represent the same material and that boundaries between materials are sharp, [Lombardi and Nishino 2012] estimate the SVBRDF of a curved object from a single image under unknown point illumination. Our method does not assume smoothness of the spatial blend or link redundant points simply by color. Another method links points by similarity in normal distribution function (NDF) over a region of overlap [Wang et al. 2008]. Dense angular sampling is required to ensure sufficient overlap.

Sparse basis Lensch et al. [2003] estimate a Lafourche model basis by progressive clustering over surface points. Their method models SVBRDFs comprising a small number of discrete BRDFs but has trouble with smooth variation. Recently, low-rank optimization has been used to jointly reconstruct both the basis BRDFs and per-point weights, as well as a spatially-varying local coordinate frame [Chen et al. 2014]. Our work adds a sparse blend constraint

to this formulation to reduce the degrees of freedom and thus the views needed.

Sparse blend The local linear model [Dong et al. 2010; Ren et al. 2011] finds the nearest basis materials and blends only them at each point. By capturing the BRDF basis in a separate pass, responses to known lighting and viewing conditions can be synthesized and compared with the physical measurements to determine which basis materials are present [Dong et al. 2010]. We generalize to an arbitrary but sparse (rather than nearby) blend, and automatically customize the representatives from a single set of measurements.

Goldman et al. [2010] solves for SVBRDFs and normal details captured under directional lighting, using a fixed number of basis materials and two blending weights per surface point. Diffuse color is used to cluster points of similar reflectance to initialize basis materials. Our method automatically determines the number of basis materials and blending weights, and works better for shiny objects by capturing them under environmental lighting without requiring material segmentation by diffuse color.

The sparse blend assumption has also been used to factorize and compress measured SVBRDF data [Lawrence et al. 2006]. Because it is formulated as a matrix factorization problem, the method requires dense (but possibly incomplete) angular measurements captured under the same lighting and viewing conditions at each point. It remains unclear how to solve for the basis and blending weights from a *sparse* set of measurements, the goal of our work. Lawrence et al. [2006] also manually determine N , make the objective sparse by an ℓ_2 norm on the set of blend weights (after excluding the one largest in magnitude), and minimize absolute reconstruction error. We solve for both N and n , directly penalize ℓ_0 sparsity, and minimize relative reconstruction error.

3 Problem Formulation

Measurement setup We acquire surface reflectance of an object of known geometry under known but passive environmental lighting by capturing images of that object from a set of k views. The object’s geometry is acquired using a previous scan. Captured images are registered using manually marked points on the object. Geometry scanning, registration and camera calibration are described more fully in Section 6. Lighting is assumed to be distant and is measured using a spherical mirror.

Surface sampling We globally parameterize the object mesh using iso-chart [Zhou et al. 2004] and represent surface points x via their (u, v) parametric coordinates in a rectangular image. Parameter space resolution is chosen manually, typically 1024×1024 , with the total number of pixels denoted M . We obtain the outgoing radiance s_x by resampling captured images from camera space into object parameter space. For each surface point x , we find its corresponding position in each of the k captured images and compute its visibility based on the known geometry. If the surface point is visible, we get the sample value by bilinearly interpolating in the captured image, taking care not to include samples that are invisible or span a depth discontinuity. If invisible, we simply record a response of 0. We finally pack the *rgb* measurements into an outgoing radiance vector, denoted \hat{s}_x , of dimensionality $K = 3k$.

Response formulation and linearity Outgoing reflectance s can be formulated as the product integral between incident lighting r and the surface BRDF P via:

$$s_x(\mathbf{o}) = \int_{\Omega_+} P_x(\mathbf{i}, \mathbf{o}) (\mathbf{n} \cdot \mathbf{i}) r_x(\mathbf{i}) d\mathbf{i} \quad (1)$$

where \mathbf{o} represents a view direction and $\mathbf{i} \in \Omega_+$ represents a lighting direction from the upper hemispherical domain. The surface normal is a constant $\mathbf{n} = (0, 0, 1)^T$ in the local frame. Spatially-varying incident radiance r_x can be inferred from the measured distant environmental lighting r and geometry.

At a particular x , we actually measure responses in just k known view directions. Assembling these responses into a single vector,

$$\mathbf{s}_x = \mathcal{R}_x(\mathbf{P}_x; \mathbf{r}_x) \quad (2)$$

where \mathbf{P}_x represents the BRDF matrix mapping incoming to outgoing radiance, \mathbf{r}_x is the incident radiance vector, and \mathbf{s}_x is the output radiance vector. The *rendering operator* \mathcal{R}_x yields the response at x of BRDF \mathbf{P}_x under incoming radiance \mathbf{r}_x in each of the k captured view directions and is obtained either through a real or synthetic measurement. Note that this operator is linear in both its arguments for any x . We will see later (Eqs. 3 and 7) that BRDFs are not explicitly represented as matrices but instead as linear combinations over a generic BRDF basis. We hereafter drop the incident radiance vector as an argument to \mathcal{R}_x , as it is understood to be derived from a single known environment map.

Synthetic measurement uses ray tracing given the BRDF, lighting, and geometry, and respects shadowing effects from the object onto itself. Inter-reflections are more challenging because they depend on the unknown reflectance as well as known geometry and are currently ignored. More details are included in Section 4.

Reflectance model We represent spatially-varying reflectance by blending between a limited set of representatives \mathbf{P}_i to obtain

$$\mathbf{P}_x = \sum_{i=1}^N \mathbf{w}_{x,i} \mathbf{P}_i \quad \left| \begin{array}{l} \|\mathbf{w}_x\|_1 = 1, \mathbf{w}_{x,i} \in [0, 1] \end{array} \right. \quad (3)$$

where $\mathbf{w}_{x,i}$ is the weight for the i -th representative BRDF at point x . The first constraint applies the ℓ_1 norm on the weight vector and forces a convex blend of representatives; i.e., the weights sum to 1. Representative BRDFs are specific to the object and are themselves formulated as a linear combination over a larger basis set of generic BRDFs as we will explain later.

Reflectance sparsity We constrain the reconstruction by penalizing N , the total number of representative BRDFs, as well as n , the maximum number of representative BRDFs that can be blended at any given surface point. Both N and n are global parameters for the entire object. We then sum the two sparsity penalties to obtain

$$\lambda_0 n + \lambda_1 N. \quad (4)$$

Choosing values for the penalty weights λ_0 and λ_1 is discussed in Section 7.

Objective We finally combine relative reconstruction error for the outgoing radiance response with our previous sparsity penalty from Eq. 4, obtaining the following overall objective to minimize:

$$\arg \min_{\mathbf{w}, \mathbf{P}_i, n, N} \sum_x \frac{\|\hat{\mathbf{s}}_x - \mathbf{s}_x\|^2}{\|\hat{\mathbf{s}}_x\|^2} + \lambda_0 n + \lambda_1 N \quad (5)$$

$$\left| \begin{array}{l} \|\mathbf{w}_x\|_1 = 1, \|\mathbf{w}_x\|_0 \leq n, \mathbf{w}_{x,i} \in [0, 1] \end{array} \right.$$

where $\hat{\mathbf{s}}_x$ is an actual radiance measurement derived from captured images and \mathbf{s}_x is a synthetic measurement defined by rendering via Eq. 2. The second constraint applies an ℓ_0 norm on the weight

vector \mathbf{w}_x to ensure that its number of non-zero components is bounded by n . Unsubscripted norms represent ℓ_2 , which always appear squared in our objectives.

4 Sparse Solver

The problem we have formulated in Eq. 5 is a challenging non-linear constrained minimization. It is high-dimensional, multiplies unknowns together in the form of blending weights and representative BRDFs, and mixes discrete and continuous variables. We iteratively solve it by alternating solution for the representative BRDFs, \mathbf{P}_i , and the weights at each surface point, \mathbf{w}_x . Sparsity parameters N and n are optimized progressively in an outer loop.

Representative optimization To compute the representative BRDFs, we fix the weights \mathbf{w}_x . Eq. 5 then becomes:

$$\arg \min_{\mathbf{P}_i} \sum_x \frac{\|\hat{\mathbf{s}}_x - \mathcal{R}_x \left(\sum_{i=1}^N \mathbf{w}_{x,i} \mathbf{P}_i \right)\|^2}{\|\hat{\mathbf{s}}_x\|^2} \quad (6)$$

after excluding irrelevant constant terms and constraints.

Representative BRDFs for the object are represented as a linear combination over a much larger set of generic BRDFs via

$$\mathbf{P}_i = \sum_{j=1}^{N^*} \mathbf{w}_{i,j}^* \mathbf{P}_j^* \quad \left| \begin{array}{l} \mathbf{w}_{i,j}^* \geq 0 \end{array} \right. \quad (7)$$

where a generic basis component is denoted \mathbf{P}_j^* from a set comprising $N^* \gg N$ members. We therefore search for the N^* N unknown weights $\mathbf{w}_{i,j}^*$ minimizing Eq. 6. This is a quadratic objective with linear inequality constraints: a QP (quadratic programming) problem. We apply our own C++ implementation of Matlab's QuadProg. Weights on the generic BRDFs \mathbf{w}^* are not constrained to sum to 1 and represent a non-negative linear combination rather than a convex blend.

Generic basis We model the generic BRDF basis $P^*(\mathbf{i}, \mathbf{o})$ using the Cook-Torrance model [Cook and Torrance 1982] via:

$$P^*(\mathbf{i}, \mathbf{o}) = \frac{D(\mathbf{h}) G(\mathbf{i}, \mathbf{o}) F(\mathbf{o} \cdot \mathbf{h})}{4(\mathbf{i} \cdot \mathbf{n})(\mathbf{o} \cdot \mathbf{n})} \quad (8)$$

where $D(\mathbf{h})$ is the microfacet normal distribution function (NDF) and \mathbf{h} the halfway direction. D is represented using the Beckmann model:

$$D(\mathbf{h}) = \frac{\exp(-\tan^2(\alpha)/\sigma^2)}{\pi \sigma^2 \cos^4(\alpha)}, \quad \alpha = \cos^{-1}(\mathbf{h} \cdot \mathbf{n}) \quad (9)$$

where σ is the roughness parameter. The shadowing and masking factor $G(\mathbf{i}, \mathbf{o})$ is given by the analytic function:

$$G(\mathbf{i}, \mathbf{o}) = \min \left(1, \frac{2(\mathbf{h} \cdot \mathbf{n})(\mathbf{i} \cdot \mathbf{n})}{\mathbf{o} \cdot \mathbf{h}}, \frac{2(\mathbf{h} \cdot \mathbf{n})(\mathbf{o} \cdot \mathbf{n})}{\mathbf{o} \cdot \mathbf{h}} \right). \quad (10)$$

The Fresnel factor $F(\mathbf{o} \cdot \mathbf{h})$ is based on Schlick's model [Schlick 1994]:

$$F(\mathbf{o} \cdot \mathbf{n}) = \tau + (1 - \tau)(1 - \mathbf{o} \cdot \mathbf{n})^5 \quad (11)$$

where τ is the Fresnel reflectance coefficient. Our generic basis then samples over the 2D space of surface roughness and Fresnel factor.

Specifically, we sample 35 different roughness values σ logarithmically distributed in the range $[0.001, 0.5]$. Schlick's model is a

convex linear combination of two components: 1 and $(\mathbf{1} - \mathbf{o} \cdot \mathbf{n})^5$. Therefore, for each roughness value we only need to sample two Fresnel coefficients, $\tau = 0$ and $\tau = 1$. We also add a purely Lambertian BRDF to the generic basis set.

The final generic basis set comprises $N^* = (35 \times 2 + 1) \times 3 = 213$ BRDF components, via the *rgb* coordinate axes $(1,0,0)$, $(0,1,0)$ and $(0,0,1)$. Each color channel of the representative basis is independent and can be solved for separately. Colored reflectance is encoded solely in the representatives; spatial blend weights in Eq. 3 are monochrome. We note that other generic BRDF basis sets can be substituted in our framework.

Blend optimization To solve for the blending weights, we fix the basis BRDFs \mathbf{P}_i as well as N and n . Each surface point x can then be solved for independently. For each surface point in sequence, we find its weight vector \mathbf{w}_x by minimizing:

$$\begin{aligned} \arg \min_{\mathbf{w}_x} & \| \hat{\mathbf{s}}_x - \mathcal{R}_x \left(\sum_{i=1}^N \mathbf{w}_{x,i} \mathbf{P}_i \right) \|^2 \\ & \left| \begin{array}{l} \|\mathbf{w}_x\|_1 = 1, \|\mathbf{w}_x\|_0 \leq n, \mathbf{w}_{x,i} \in [0, 1]. \end{array} \right. \end{aligned} \quad (12)$$

The weight summation constraint $\|\mathbf{w}_x\|_1 = 1$ can be eliminated by the trick of setting the last weight value as $\mathbf{w}_{x,N} = 1 - \sum_{i=1}^{N-1} \mathbf{w}_{x,i}$, and reducing the degrees of freedom by one. However, the discrete nature of the n -way spatial blend makes the system hard to solve. It is practical to apply a brute force strategy for the relatively small values of n required in real examples, usually no more than 5. Knowing which n elements of \mathbf{w}_x are non-zero converts the problem to a (purely continuous) quadratic programming problem. We try all possible combinations of n nonzero basis BRDFs chosen from the N representatives, and find the minimal among them. Section 6 proposes a method to reduce the number of candidates.

Precomputed rendering The representative BRDF and weight optimization steps both involve synthesizing the outgoing radiance response from an unknown linear combination of known BRDFs. We can accelerate the computation by exploiting the linear nature of the rendering operator, for which $\mathcal{R}_x \left(\sum_j \mathbf{w}_j^* \mathbf{P}_j^* \right) = \sum_j \mathbf{w}_j^* \mathcal{R}_x(\mathbf{P}_j^*)$. Assuming the geometry and environmental light are fixed, we precompute rendering results for each generic BRDF basis component j , yielding N^* K -channel images

$$\mathbf{s}_{x,j}^* = \mathcal{R}_x(\mathbf{P}_j^*). \quad (13)$$

These are stored in the object's parameter space, matching the resampled images of captured radiance, $\hat{\mathbf{s}}_x$, and allowing easy solution of Eq. 6 in terms of sum of squared pixel differences over images. Similarly, at the start of each weight optimization, we update rendered images for each representative BRDF i by computing the weighted combination of generic basis renderings. Eq. 7 yields

$$\mathbf{s}_{x,i} = \mathcal{R}_x(\mathbf{P}_i) \Rightarrow \mathbf{s}_{x,i} = \sum_{j=1}^{N^*} \mathbf{w}_{i,j}^* \mathbf{s}_{x,j}^*. \quad (14)$$

We can then solve Eq. 12 in terms of sum of squared K -channel pixel differences between $\hat{\mathbf{s}}_x$ and linear combinations of these $\mathbf{s}_{x,i}$.

Optimizing n and N We optimize n and N by brute force search in the outer loop of the optimization. Starting from 1, we progressively increment n . For each n , we progressively increment N also

starting from 1. In either loop, we terminate the search when the objective first increases and chose the preceding value of N or n . This is not a globally optimal solution, but produces good results in our experiments.

Initialization Starting at $N = 1$, we initialize the per-surface blending weight as $\mathbf{w}_x = \mathbf{1}$ and perform representative optimization to find the single corresponding representative. Then in each iteration that increments N by 1, we apply the following, admittedly ad hoc procedure. We select surface points with relative fitting error larger than a threshold λ_N and optimize using only this subset to compute a single, newly-added representative with blending weight $\mathbf{w}_{x,N} = \mathbf{1}$ at those points. Other points retain the blending weights they had before on the old representatives, with zero weight on this newly added representative. The threshold begins at $\lambda_1 = 0.1$ and progressively decreases via $\lambda_{N+1} = 0.8 \lambda_N$.

5 Analysis

Quadratic objectives in Eqs. 6 and 12 correspond to (over-constrained) linear systems. It is useful to describe these so we can analyze solution robustness in terms of matrix conditioning/rank. This analysis ignores constraints, focusing instead on the objective gradient to which this linear system is directly related.

Linear systems Representative optimization (Eqs. 7 and 6) can be rewritten:

$$\arg \min_{\mathbf{w}^*} \sum_x \gamma_x \| \hat{\mathbf{s}}_x - \sum_{i=1}^N \sum_{j=1}^{N^*} \mathbf{w}_{x,i} \mathbf{w}_{i,j}^* \mathbf{s}_{x,j}^* \|^2 \quad (15)$$

where $\hat{\mathbf{s}}_x$, $\mathbf{w}_{x,i}$, and $\mathbf{s}_{x,j}^*$ are fixed, and $\gamma_x = \|\hat{\mathbf{s}}_x\|^{-2}$. The linear system associated with this quadratic objective has KM rows (constraints where a radiance response must be matched) and NN^* columns (unknown component of the weight matrix \mathbf{w}^*).

Blend optimization at a given x (Eq. 12) can be rewritten:

$$\arg \min_{\mathbf{w}_x} \| \hat{\mathbf{s}}_x - \sum_{i=1}^N \mathbf{w}_{x,i} \mathbf{s}_{x,i} \|^2. \quad (16)$$

The linear system associated with this quadratic objective has K rows and N columns.

At a given pixel x , generic and representative basis renderings form the $K \times N^*$ matrix $\mathbf{s}_x^* = [\mathbf{s}_{x,1}^*, \mathbf{s}_{x,2}^*, \dots, \mathbf{s}_{x,N^*}^*]$ and the $K \times N$ matrix $\mathbf{s}_x = [\mathbf{s}_{x,1}, \mathbf{s}_{x,2}, \dots, \mathbf{s}_{x,N}]$, respectively. Generic weights \mathbf{w}^* form a $N \times N^*$ matrix while blend weights \mathbf{w}_x form an N -dimensional vector. Eq. 14 can then be rewritten

$$\mathbf{s}_x = \mathbf{s}_x^* \mathbf{w}^{*T}. \quad (17)$$

With these definitions, Eq. 16 yields the derived linear system

$$\mathbf{s}_x \mathbf{w}_x = \hat{\mathbf{s}}_x, \quad (18)$$

while Eq. 15 yields the derived linear system at each x

$$\gamma_x \mathbf{s}_x^* \cdot \mathbf{w}^* = \hat{\mathbf{s}}_x. \quad (19)$$

The $a \cdot b$ operator above represents the sum of products over all $N \times N^*$ components of its two matrix operands and \mathbf{s}_x^* is the $K \times N \times N^*$ tensor given by

$$\begin{aligned} \mathbf{s}_x^* &= \gamma_x \mathbf{w}_x \otimes \mathbf{s}_x^* \\ &= \gamma_x \begin{bmatrix} \mathbf{w}_{x,1} \mathbf{s}_{x,1}^* & \mathbf{w}_{x,1} \mathbf{s}_{x,2}^* & \dots & \mathbf{w}_{x,1} \mathbf{s}_{x,N^*}^* \\ \mathbf{w}_{x,2} \mathbf{s}_{x,1}^* & \mathbf{w}_{x,2} \mathbf{s}_{x,2}^* & \dots & \mathbf{w}_{x,2} \mathbf{s}_{x,N^*}^* \\ \vdots & \vdots & \ddots & \vdots \\ \mathbf{w}_{x,N} \mathbf{s}_{x,1}^* & \mathbf{w}_{x,N} \mathbf{s}_{x,2}^* & \dots & \mathbf{w}_{x,N} \mathbf{s}_{x,N^*}^* \end{bmatrix}. \end{aligned} \quad (20)$$

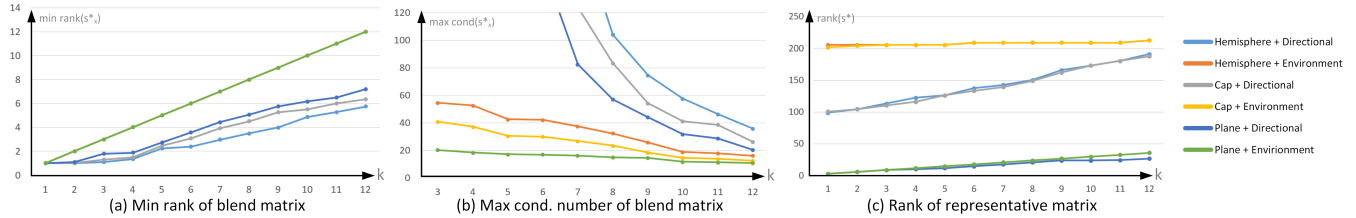


Figure 2: Linear system robustness as a function of the number of captured views k . We compare 6 experimental situations varying both lighting and geometry (legend at far right), using three measures of robustness: worst-case rank (a) and condition number (b) of the blend matrix, and rank of the representative matrix (c). The green curve in (a) actually overlies the red and yellow ones, as well as the result using the optimized direction set of [Nielsen et al. 2015] (not shown in legend).

To convert this into proper matrix form, we simply rearrange \mathbf{w}^* into a 1D vector, denoted $\tilde{\mathbf{w}}^*$, and concatenate all N rows of \mathbf{s}_x^* into one, forming the $K \times NN^*$ matrix $\tilde{\mathbf{S}}_x^*$.

Matrix rank analysis For blend optimization, the constraints $\|\mathbf{w}_x\|_0 = n$ and $\|\mathbf{w}_x\|_1 = 1$ imply that \mathbf{w}_x has $n - 1$ degrees of freedom. By Eq. 18, \mathbf{s}_x must have rank at least $n - 1$ to sufficiently constrain these. Then by Eq. 17, \mathbf{s}_x^* must have rank at least $n - 1$. We call \mathbf{s}_x^* the *blend optimization matrix*.

For representative optimization, aggregating equality constraints across pixels combines rows of $\tilde{\mathbf{S}}_x^*$ over every x to form an $MK \times NN^*$ matrix $\tilde{\mathbf{S}}^*$. This matrix must be full rank for the linear system in Eq. 15 to sufficiently constrain the degrees of freedom in $\tilde{\mathbf{w}}^*$. Any columns selected from it must be linearly independent. If we select those columns related to a single representative BRDF i (i.e., a single row of the weight matrix, \mathbf{w}_i^*), the resulting submatrix should have rank N^* . From Eq. 20, we see that a row in this submatrix is scaled by the same value $\gamma_x \mathbf{w}_{x,i}$ which can be removed without changing the rank. We finally obtain the $KM \times N^*$ matrix

$$\mathbf{s}^* = \begin{bmatrix} \mathbf{s}_{x_1,1}^* & \mathbf{s}_{x_1,2}^* & \cdots & \mathbf{s}_{x_1,N^*}^* \\ \mathbf{s}_{x_2,1}^* & \mathbf{s}_{x_2,2}^* & \cdots & \mathbf{s}_{x_2,N^*}^* \\ \vdots & \vdots & \vdots & \vdots \\ \mathbf{s}_{x_M,1}^* & \mathbf{s}_{x_M,2}^* & \cdots & \mathbf{s}_{x_M,N^*}^* \end{bmatrix} \quad (21)$$

whose rank must be N^* (full) to determine a unique solution for any \mathbf{w}_i^* . We call \mathbf{s}^* the *representative optimization matrix*.

Note that both rank conditions derived above are necessary but not sufficient, allowing analysis that depends only on the generic basis and not the unknown set of representative BRDFs or the spatial blending weights. The importance of the two matrices is clear intuitively: we must be able to linearly separate responses for each of the generic basis components, both at each x and over the object as a whole, in order to compute their optimal linear combination.

Application Using these tools, we experimentally study how lighting (environmental vs. directional) and object geometry (plane vs. spherical cap vs. hemisphere) affect linear system robustness as k grows. Results are shown in Figure 2. The normal map of the plane samples a single direction while the cap and hemisphere cover a solid angle of π and 2π respectively. Blend matrix results (in a and b) summarize worst case over all x ; i.e., minimum rank and maximum condition number. For directional lighting, we choose a random light and view direction in each trial and average over 80 trials. For environment map (EM) lighting, we again average over 80 trials: four EMs (St.Peters, Grace, Grove and Uffizi from [Debevec 1998]) \times 20 trials picking a random EM rotation and view vector for each EM.

A directional light point-samples the surface BRDF. On shiny surfaces, all angular variation occurs near the reflection direction and is easy to miss. Figure 2a shows that the minimum rank of \mathbf{s}_x^* grows slowly with increasing k for randomly-selected directional lighting, regardless of the geometry. Environmental lighting yields more response variation and thus faster growth in rank. This result is confirmed by an analysis of condition number, shown in (b), where smaller is better. Our analysis assumes $n=4$, so the required condition number of \mathbf{s}_x^* is computed as the ratio of its maximum singular value over the third ($n - 1$) biggest.

Since all \mathbf{s}_x^* are identical on the plane, one can choose special sets of light and view directions [Nielsen et al. 2015, Table 1] to produce a high rank matrix. The resulting curve superimposes over the (best) green curve in (a), along with the three curves for environmental lighting. In other words, by carefully rather than arbitrarily choosing a light/view directions, we can obtain results equivalent to environmental lighting, based on the blend matrix. Environmental lighting is still superior to directional for representative matrix analysis with curved geometries, shown in (c). In this case, the surface normal varies with x and it becomes unclear how to choose optimal light/view directions. We conclude that natural, environmental lighting is superior to directional for reflectance acquisition.

Shape also affects robustness. While condition number analysis of the blend matrix (in b) finds the three geometries (plane, cap, and hemisphere) similarly robust, rank analysis of the representative matrix (in c) significantly favors curved geometry over flat, especially for small k . Results are similar for the cap and hemisphere: while some normal variation is critical, complete coverage is unnecessary.

6 Implementation

We implemented our reconstruction algorithm on an Intel Xeon E5-2630 V3 workstation with 64GB of memory. The object's shape was first captured using an Artec Space Spider 3D scanner, and reflectance images were acquired by a Canon EOS 5D Mark III digital camera with EF 70-200F4L lens. Luminance measurements were linearized by converting 14-bit RAW image values using the radiance response curve supplied in the RAW file. We calibrated the intrinsic parameters of the camera using the method of Zhang et al. [2000]. Environmental lighting was captured with a spherical mirror. To manipulate the view, we manually move the camera mounted on a tripod. Capture takes less than 10 minutes including setup. Reconstruction time ranges from 20 to 380 minutes depending on k and the target's reflectance complexity.

Registration We align the shape in the first captured frame by manually marking corresponding points in the image and on the geometry. We then apply ICP to determine the rigid transformation

aligning the geometry to its pose in the captured image. Correspondences between images are provided by SIFT features [Lowe 1999]. The environment map is captured with the same view as the first captured frame, allowing us to infer its orientation with respect to the target. For objects without significant texture (like DustSph), we place an additional checker pattern in the scene to infer camera pose. For spherical shapes, we skip the step of pre-scanning the geometry and simply align silhouettes.

Search pruning Optimizing blending weights via Eq. 12 involves a brute-force search of all combinations of n representatives from the N available. Computation increases exponentially as N and n increase. To reduce it, we precompute a smaller set of combinations by performing the full search on a randomly selected subset of 5% of surface pixels. We further remove outliers by culling basis combinations to cover 99% of those sampled pixels. The basis combination search space is updated before each iteration. To make sure optimization progresses downhill, we also add for each pixel the single basis combination selected for it in the previous iteration.

7 Results

Rendered images appearing in figures apply fixed gamma correction (of 2.2) and a constant exposure setting normalized by average intensity of the environment map (EM). Quantitative image error in figures and plots is measured in linear space without tone mapping or exposure manipulation, in terms of square root of sum of squared error normalized by sum of squares of the reference image (NRMS), and considering only foreground pixels covered by the target object.

7.1 Synthetic validation

Experiments measure image error after applying the Uffizi EM, different from the one applied in synthetic capture (typically Grace or St. Peters). In experiments that vary k , input views are randomly generated from a uniform spherical distribution with all methods sharing the same initial subsequence of views from this randomly-generated sequence.

Number of views We created a synthetic target mapping the “copper” SVBRDF from [Wang et al. 2008] onto a sphere. Simulating capture in the Grace EM, we measured reconstruction error in rendered image space as a function of the number of views. Figure 3 shows visual reconstruction quality for $k=5$ and $k=10$, while Figure 4 plots quantitative image error with increasing k . Error is averaged over 10 trials that randomly choose the views. Note the significant “knee” in the curve at $k=3$, after which error levels off.

Sparseness penalty values We investigated how sparseness penalty weights, λ_0 and λ_1 , affect reconstruction quality using the same “copper” target used in the previous experiment. Fixing $k=10$, we ran the solver with penalty weights varying in the range $\lambda_0 \in [0.003^2, 0.01^2]$ and $\lambda_1 \in [0.001^2, 0.005^2]$. The algorithm produced very similar results, both visually and in terms of quantitative image error, with NRMS image error smaller than 5% in all cases. Underweighting the sparseness penalty overfits the data with an unduly complicated model and yields poor reconstruction in novel situations. Overweighting it yields a high-error reconstruction to the given measurements. But a wide range of intermediate penalties yield good results.

Search pruning Using the copper SVRBDF and Grace EM again, we compare results by brute-force search of basis combi-

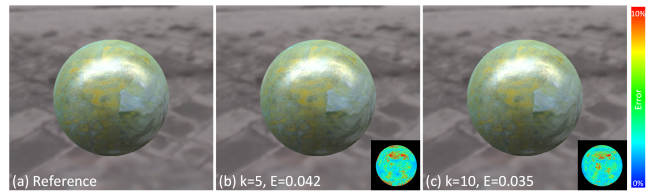


Figure 3: “Copper” validation, $k=5$ (b) and $k=10$ (c). Error color-coded in inset.

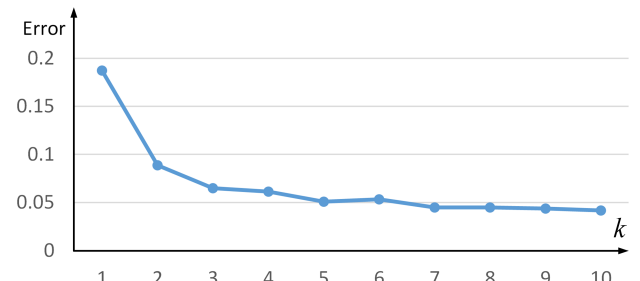


Figure 4: “Copper” error as a function of k .

nations against our proposed pruning. We obtain similar fidelity using 47% less computation, as shown in Figure 5, which applies two novel EMs in the rendering (Uffizi and Grove).

Sparseness effectiveness To isolate the effects of our two sparseness terms, we perform reconstruction with only one or the other by setting $\lambda_0 = 0$ or $\lambda_1 = 0$. We designed a synthetic SVBRDF with known sparseness by choosing four materials from the MERL database [Matusik et al. 2003] (*pink-plastic*, *hematite*, *yellow-phenolic* and *blue-metallic-paint*), and blending two of them at each surface point. The ground truth is thus $n=2$ and $N=4$. We applied this material to a sphere and simulated capture in the St. Peters EM.

As shown in Figure 6, our method with both terms achieves excellent visual quality and low NRMS error with $k=6$ views. Without the sparse basis term, the number of basis components freely increases until it uses the entire generic basis as representatives, entailing many more degrees of freedom. Not surprisingly, many more views $k=75$ are then required to achieve equal quality results. Removing the sparse blend term allows $n=N$; this is equivalent to a global linear model. Again, more views $k=12$ are required to determine the additional weights per surface point.

Comparison to existing methods The global linear method [Chen et al. 2014] is also based on the sparse basis assumption but lacks our sparse blend prior. As shown in Figure 6c using reconstruction code supplied by the authors, it produces poor results for small k , requiring a much bigger $k=62$ for an equal-quality reconstruction. Even without exploiting the sparse blend assumption, our method needs fewer views ($k=12$) to achieve an equal-quality reconstruction. This is because our method directly minimizes N whereas Chen applies an approximate ℓ_0 norm (based on the nuclear norm of \mathbf{w}^*) that over-estimates it, enlarges the basis set, and so requires more measurements. Specifically, our method with only the sparse basis term yields the ground truth number of representatives $N=4$, whereas [Chen et al. 2014] yields $N=9$. Including the sparse blend term then further improves our reconstruction.

Goldman et al. [2010] proposed a method with similar but less general sparseness assumptions: they assume the material is com-

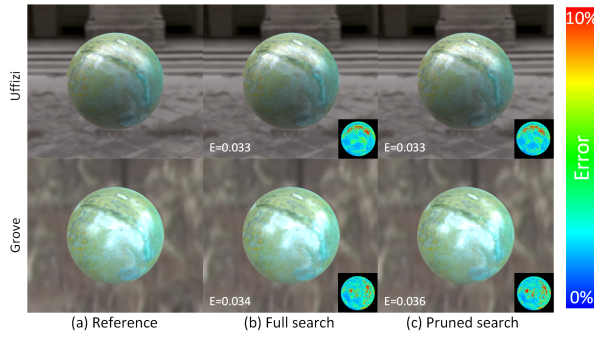


Figure 5: Accelerated basis search. Reconstruction results by (b) brute-force search, and (c) pruned search are compared with the reference (a). Pruning produces similar quality in about half the computation time. Error is visualized in the inset.

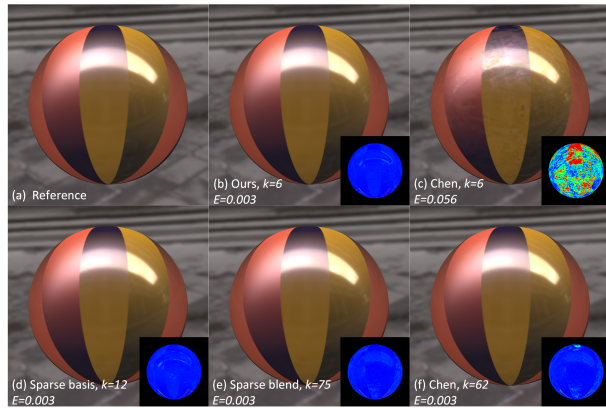


Figure 6: Sparseness effectiveness. Our method (b) needs only $k=6$ views to achieve good visual quality and small quantitative error on this synthetic example. Retaining only the sparse basis (d) or the sparse blend term (e) alone requires more views ($k=12$ or $k=75$) to get equal quality results. The global linear method [Chen et al. 2014] yields poor quality for $k=6$ (c), requiring $k=62$ views (f) to match our quality.

posed of a known number of representatives in which $n=2$ of them are blended at each surface point. To compare our method, we chose two datasets which intentionally break the $n=2$ assumption, one synthetic and one measured. The synthetic SVBRDF blends between $n=3$ BRDFs chosen from our generic basis with different diffuse/specular colors and roughness values, via barycentric interpolation over a spherically-projected equilateral triangle. The measured SVBRDF is the “copper” dataset from [Wang et al. 2008]. Since [Goldman et al. 2010] only supports directional lighting, we perform its synthetic capture with randomly placed directional lights distributed uniformly over the sphere. We use our own implementation of Goldman’s method, which fixes rather than reconstructs the known lighting and (spherical) normals. It tries $N \in \{5, 10, 15, 20, 25\}$ and selects the result having lowest error. We test two variants of our method, one fixed at $n=2$ and one with n free, using images captured under the St. Peters EM. Figure 7 shows that a restricted $n=2$ blend fails to represent these materials. Because it’s further limited by directional lighting, [Goldman et al. 2010] requires even more measurements while producing results with larger reconstruction error.

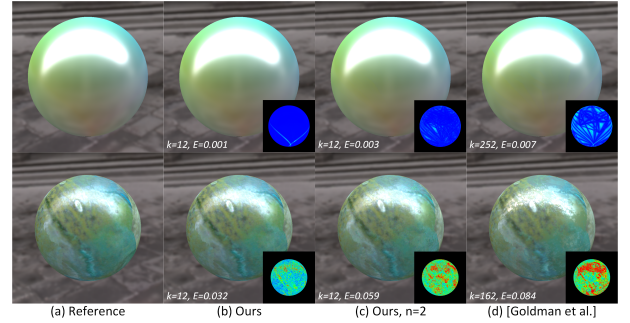


Figure 7: Comparison with [Goldman et al. 2010]. The top row represents a synthetic material while the bottom is a measured one. Our method (b) needs $k=12$ views to achieve good quality results. Forcing the blend sparsity at $n=2$ in (c) yields larger quantitative error. By using directional light sources, [Goldman et al. 2010] in (d) requires even more measurements k while yielding still larger error.

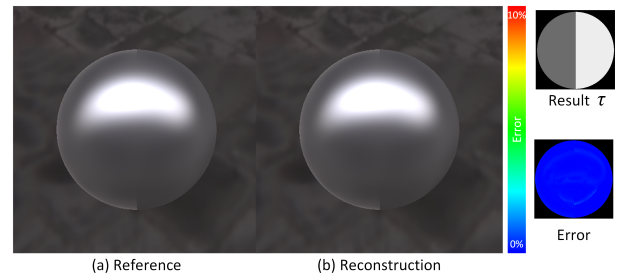


Figure 9: Fresnel validation. The left and right halves of this synthetic target differ only in Fresnel coefficient, τ . Our reconstruction accurately captures this subtle variation.

Generic basis sufficiency and EM capture independence
With each of the 100 MERL materials [Matusik et al. 2003] mapped homogeneously over a sphere, we simulated the capture of a single image in the Grace and St. Peters EMs, and computed rendered reconstruction error in Grove and Uffizi. A selection of results are shown in Figure 8, with images for all MERL materials available in the supplement. Two main observations can be made. One is that our generic basis works well: we get excellent visual and quantitative fidelity for all 100 MERL materials. The second is that our method’s reconstruction quality does not significantly depend on which EM was used in the synthetic capture, as long as it is natural and complex.

Fresnel recovery We designed a spherical target consisting of two materials differing only by Fresnel parameter: $\tau=0.15$ (left side) and $\tau=0.85$ (right side). We adapt the specular coefficient ρ_s on each side so as to normalize BRDF response for lighting incident in the surface normal direction. Both sides have the same roughness, $\sigma=0.165$. We synthetically capture applying the Grace EM using $k=8$ random views. Figure 9 shows our method’s ability to faithfully recover τ in this challenging case.

Error sensitivity Geometry and image registration accuracy obviously affect reconstruction quality. We simulate geometry error by perturbing each surface normal randomly. We tested four homogeneous spheres of different roughness, in the range $\sigma \in [0.05, 0.20]$. Figure 10 plots reconstruction error in image space as a function of perturbation amplitude measured as the average an-

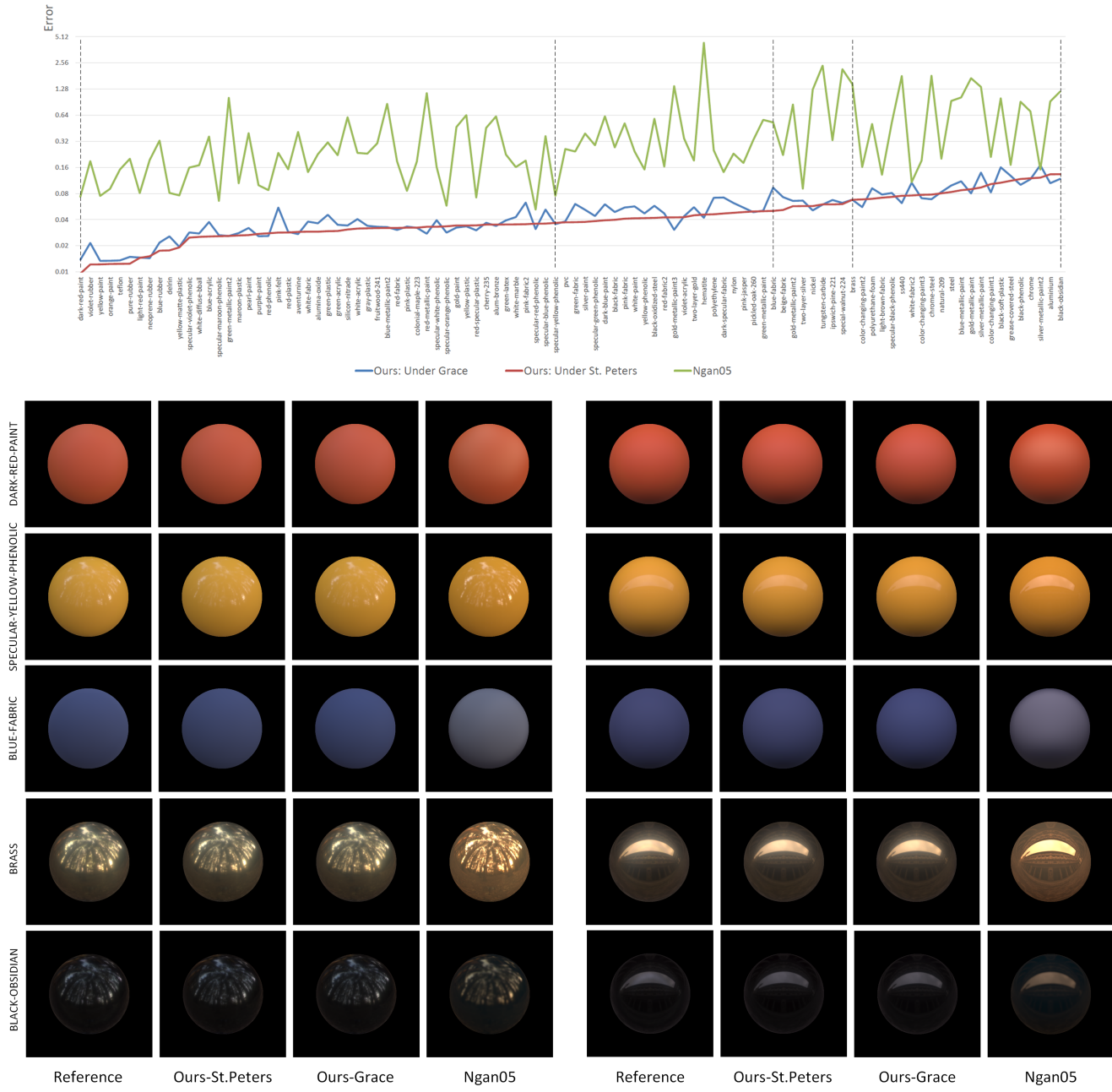


Figure 8: MERL dataset validation. Applying each MERL material to a homogeneous sphere, we perform synthetic capture under the St. Peters and Grace EMs. We show images of our reconstructed results compared with the reference and the fit of [Ngan et al. 2005] under two novel EMs: Grove (left four images) and Uffizi (right four). Rendering error for all 100 MERL BRDFs is plotted at the top (note log scale), averaged over the Grove and Uffizi EMs.

gle between the perturbed normal and the actual one. Figure 11 shows the effect of error in camera position. We apply uniform random noise to the camera position (measured as a percentage of the camera’s distance to the object) while keeping the camera pointed at the target’s center, and plot image error as a function of noise amplitude. Not surprisingly, shinier materials are more sensitive to error in both experiments.

Object	k	n	N	time (mins)
Bear	1	1	10	12
Kitty	5	2	8	123
Billiard	20	2	6	152
PaintSph	17	5	6	280
Pig	54	4	8	310
Mouse	26	3	9	253
DustSph	22	3	5	190
CopperPlt	45	5	18	298

Table 1: Real object capture data.

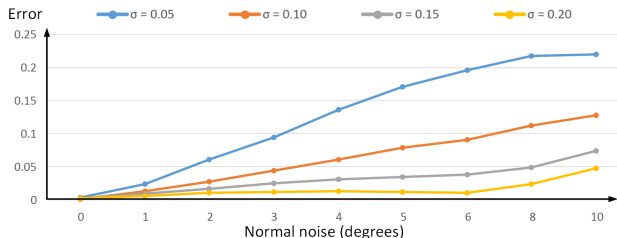


Figure 10: Normal error sensitivity.

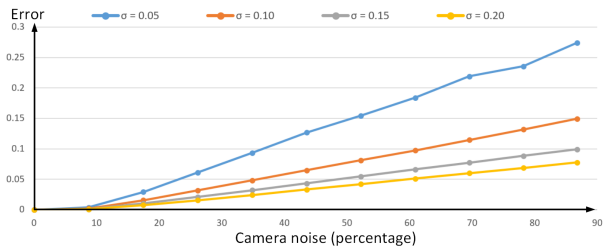


Figure 11: Camera error sensitivity.

7.2 Real object capture

We captured reflectance from eight real objects with data summarized in Table 1. The EM acquired for each target is shown in Figure 12. In practice, we manually place views to distribute them roughly uniformly around the object. Note that the required number of views, k , is affected by many properties of the acquisition target’s geometry and reflectance (e.g. surface visibility, reflectance complexity and redundancy), and the lighting. Using the analysis from Section 5, with geometry and lighting fixed, we can determine k by increasing it until reaching a desired condition number on the blend and representative optimization matrices.

Figure 15 visualizes some reflectance properties of the objects we acquired. We observed little spatial variation in acquired τ in these examples.

Bear and Kitty comprise a number of different basic materials ($N=10$ for Bear and $N=8$ for Kitty) piecewise-distributed with little blending. Our method efficiently reconstructs such objects with a minimal number of measurements, by restricting itself to a suitably sparse blend. The Billiard example combines a similar patchwork with gradual shininess variation corresponding to a wear pattern. Our model reproduces both sharp material boundaries and large-scale smooth variation. The PaintSph, DustSph and CopperPlt targets exhibit rich material variation and textural detail and span the range of specularity from mirror-like (part of DustSph), through glossy (PaintSph), to rough (CopperPlt). The Pig mixes complicated geometry (e.g. headcloth, ears) and non-trivial material variation, while the Mouse exhibits material discontinuities as well as smoother smudging and wear. Representative BRDFs and the blending weight map can be found in the supplementary material.

Figure 13 compares reconstruction on the Kitty model for $k=1$ and $k=5$. Single-image reconstruction provides good results. Transitions between materials and details around the kitty’s whiskers are improved using more views. Note that our method automatically adapts n as the input k is changed.

We captured photos of each object under lighting different from that used in acquisition, and compare these photos with renderings of our reconstruction in Figure 14. The novel lighting we apply

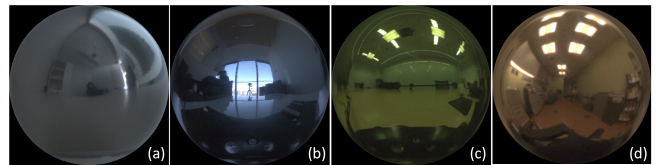


Figure 12: Capture EMs for real objects: (a) Bear and Kitty; (b) Billiard and PaintSph; (c) Pig, DustSph and CopperPlt; (d) Mouse.



Figure 13: Single vs. multiple measurements.

was captured with a spherical mirror, as in reflectance acquisition. Overall reconstruction quality is shown by applying novel lighting in Figures 1 and 16, and in our video results.

8 Conclusion

By modeling reflectance variation using a small set of representative materials, an even smaller number of which are convexly blended at each surface point, we obtain a faithful SVBRDF reconstruction using surprisingly few captured views. We designed a sparse solver to jointly compute the representatives and spatial blend weights, based on an objective that considers relative fidelity to the sparse measurements and directly penalizes the number of representatives and maximum number of them to blend. Our method is automatic and avoids predetermined the representatives or linking points via simplistic assumptions on spatial correlation. It requires many fewer views than the global linear method. Notions of the generic basis and linear systems we develop let us evaluate how capture factors such as lighting and target shape affect reconstruction robustness and the minimal number of views it demands.

Our method works well for a wide range of materials including ones with spatially-varying glossiness and even microfacet-based Fresnel behavior, but has several limitations. It ignores anisotropic BRDFs and subsurface scattering effects. It depends on the generic basis, though we have shown that our choice reconstructs real-world isotropic materials from the MERL database accurately. It assumes surface geometry is known and registration between images and geometry is accurate. In future work, we’d like to speed up our reconstruction algorithm, explore other (perhaps nonlinear) generic BRDF representations, extend to active lighting, and capture anisotropic BRDFs and normal maps.

Acknowledgements

The authors wish to thank the reviewers for their constructive feedback, also thank Wojciech Matusik for providing the MERL BRDF database. The 3D geometry scan service is provided by Beijing Asahi 3D Technology Co.,Ltd.

References

- AITTALA, M., WEYRICH, T., AND LEHTINEN, J. 2013. Practical SVBRDF capture in the frequency domain. *ACM Trans. Graph.* 32, 4 (July), 110:1–110:12.
- AITTALA, M., WEYRICH, T., AND LEHTINEN, J. 2015. Two-shot SVBRDF capture for stationary materials. *ACM Trans. Graph.* 34, 4 (July), 110:1–110:13.
- CHEN, G., DONG, Y., PEERS, P., ZHANG, J., AND TONG, X. 2014. Reflectance scanning: Estimating shading frame and BRDF with generalized linear light sources. *ACM Transactions on Graphics* 33, 4 (August).
- COOK, R. L., AND TORRANCE, K. E. 1982. A Reflectance Model for Computer Graphics. *ACM Trans. Graph.* 1, 1, 7–24.
- DEBEVEC, P. 1998. Rendering synthetic objects into real scenes: Bridging traditional and image-based graphics with global illumination and high dynamic range photography. In *Proceedings of the 25th Annual Conference on Computer Graphics and Interactive Techniques*, ACM, New York, NY, USA, SIGGRAPH '98, 189–198.
- DONG, Y., WANG, J., TONG, X., SNYDER, J., LAN, Y., BEN-EZRA, M., AND GUO, B. 2010. Manifold bootstrapping for SVBRDF capture. *ACM Trans. Graph.* 29, 4 (July), 98:1—98:10.
- DONG, Y., CHEN, G., PEERS, P., ZHANG, J., AND TONG, X. 2014. Appearance-from-motion: Recovering spatially varying surface reflectance under unknown lighting. *ACM Trans. Graph.* 33, 6 (Nov.), 193:1–193:12.
- GARDNER, A., TCHOU, C., HAWKINS, T., AND DEBEVEC, P. 2003. Linear light source reflectometry. *ACM Trans. Graph.* 22, 3 (July), 749–758.
- GOLDMAN, D., CURLESS, B., HERTZMANN, A., AND SEITZ, S. 2010. Shape and spatially-varying brdfs from photometric stereo. *Pattern Analysis and Machine Intelligence, IEEE Transactions on* 32, 6 (June), 1060–1071.
- LAWRENCE, J., BEN-ARTZI, A., DECORO, C., MATUSIK, W., PFISTER, H., RAMAMOORTHI, R., AND RUSINKIEWICZ, S. 2006. Inverse shade trees for non-parametric material representation and editing. *ACM Trans. Graph.* 25, 3 (July), 735–745.
- LENSCH, H. P. A., KAUTZ, J., GOESELE, M., HEIDRICH, W., AND SEIDEL, H.-P. 2003. Image-based reconstruction of spatial appearance and geometric detail. *ACM Trans. Graph.* 22, 2 (Apr.), 234–257.
- LOMBARDI, S., AND NISHINO, K. 2012. Single image multitematerial estimation. In *Proceedings of the 2012 IEEE Conference on Computer Vision and Pattern Recognition (CVPR)*, IEEE Computer Society, Washington, DC, USA, CVPR '12, 238–245.
- LOWE, D. G. 1999. Object recognition from local scale-invariant features. In *Proceedings of the International Conference on Computer Vision-Volume 2 - Volume 2*, IEEE Computer Society, Washington, DC, USA, ICCV '99, 1150–.
- MATUSIK, W., PFISTER, H., BRAND, M., AND McMILLAN, L. 2003. A data-driven reflectance model. *ACM Transactions on Graphics* 22, 3 (July), 759–769.
- MCALLISTER, D. K. 2002. *A Generalized Surface Appearance Representation for Computer Graphics*. PhD thesis. AAI3061704.
- NGAN, A., DURAND, F., AND MATSIK, W. 2005. Experimental analysis of BRDF models. In *Proceedings of the Eurographics Symposium on Rendering*, Eurographics Association, 117–226.
- NIELSEN, J. B., JENSEN, H. W., AND RAMAMOORTHI, R. 2015. On optimal, minimal brdf sampling for reflectance acquisition. *ACM Trans. Graph.* 34, 6 (Oct.), 186:1–186:11.
- REN, P., WANG, J., SNYDER, J., TONG, X., AND GUO, B. 2011. Pocket reflectometry. *ACM Trans. Graph.* 30, 4 (July), 45:1—45:10.
- SCHLICK, C. 1994. An inexpensive BRDF model for physically-based rendering. *Computer Graphics Forum* 13, 3, 233–246.
- WANG, J., ZHAO, S., TONG, X., SNYDER, J., AND GUO, B. 2008. Modeling anisotropic surface reflectance with example-based microfacet synthesis. *ACM Trans. Graph.* 27, 3 (Aug.), 41:1—41:9.
- ZHANG, Z. 2000. A flexible new technique for camera calibration. In *IEEE PAMI*, vol. 22, 1330–1334.
- ZHOU, K., SYNDER, J., GUO, B., AND SHUM, H.-Y. 2004. Iso-charts: Stretch-driven mesh parameterization using spectral analysis. In *Proceedings of the 2004 Eurographics/ACM SIGGRAPH Symposium on Geometry Processing*, ACM, New York, NY, USA, SGP '04, 45–54.
- ZICKLER, T., ENRIQUE, S., RAMAMOORTHI, R., AND BEL-HUMEUR, P. 2005. Reflectance sharing: image-based rendering from a sparse set of images. In *Proceedings of the Sixteenth Eurographics conference on Rendering Techniques*, Eurographics Association, Aire-la-Ville, Switzerland, Switzerland, EGSR'05, 253–264.

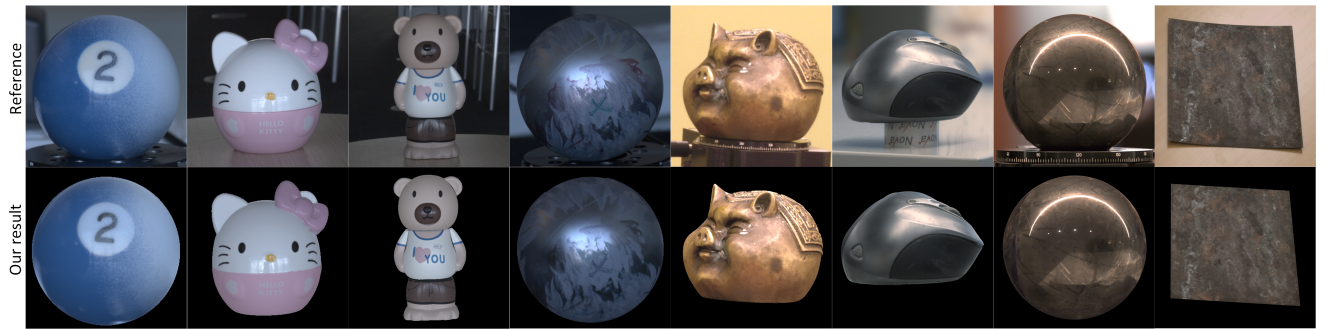


Figure 14: Visual comparison under novel lighting. We compare our reconstruction (bottom) to a reference photograph (top) under lighting that differs from the acquisition environment.

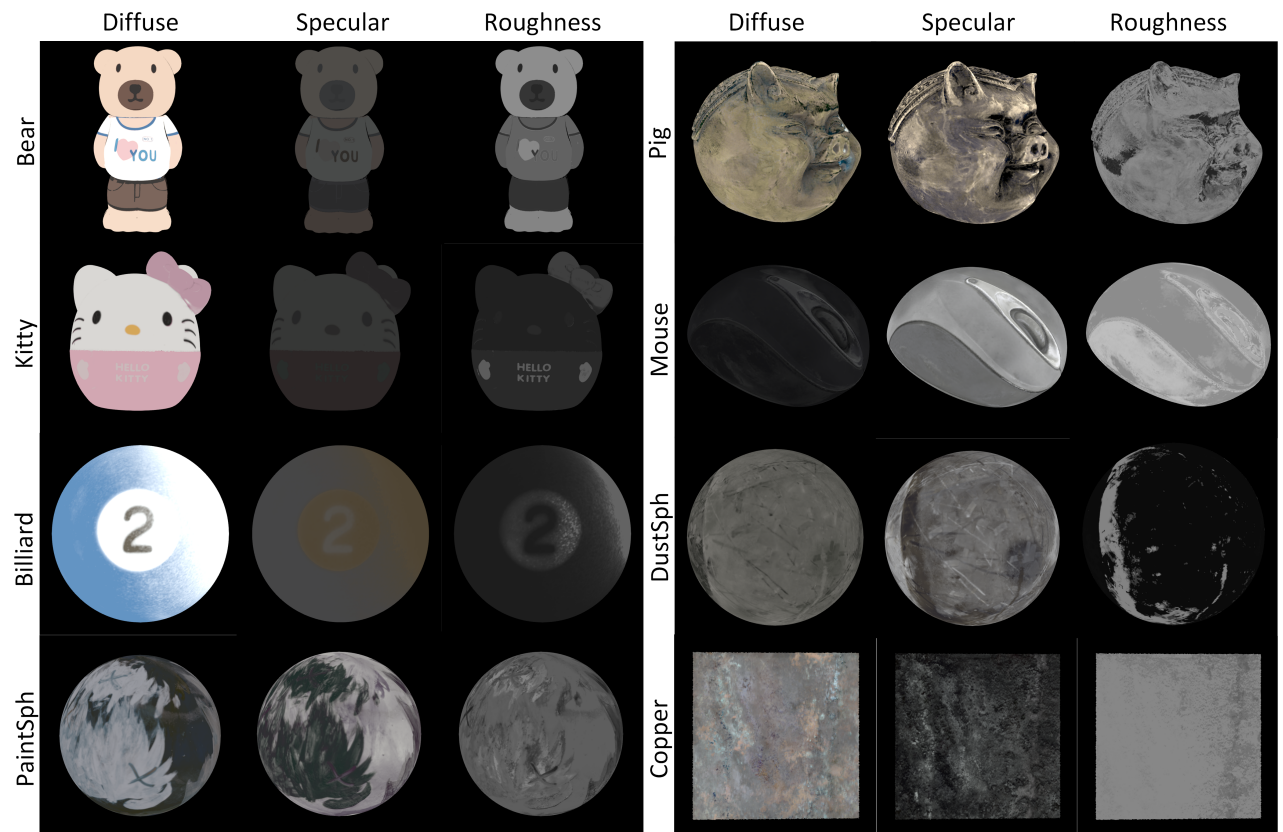


Figure 15: Recovered reflectance properties. For visualization, we fit the NDF with a single Beckmann lobe and show the fitted roughness. In fact our representation is more complex, and is instead given by a linear combination over our generic basis. Diffuse and specular coefficients are separated using the Lambertian component included in our generic basis. Full material maps can be found in the supplementary materials.

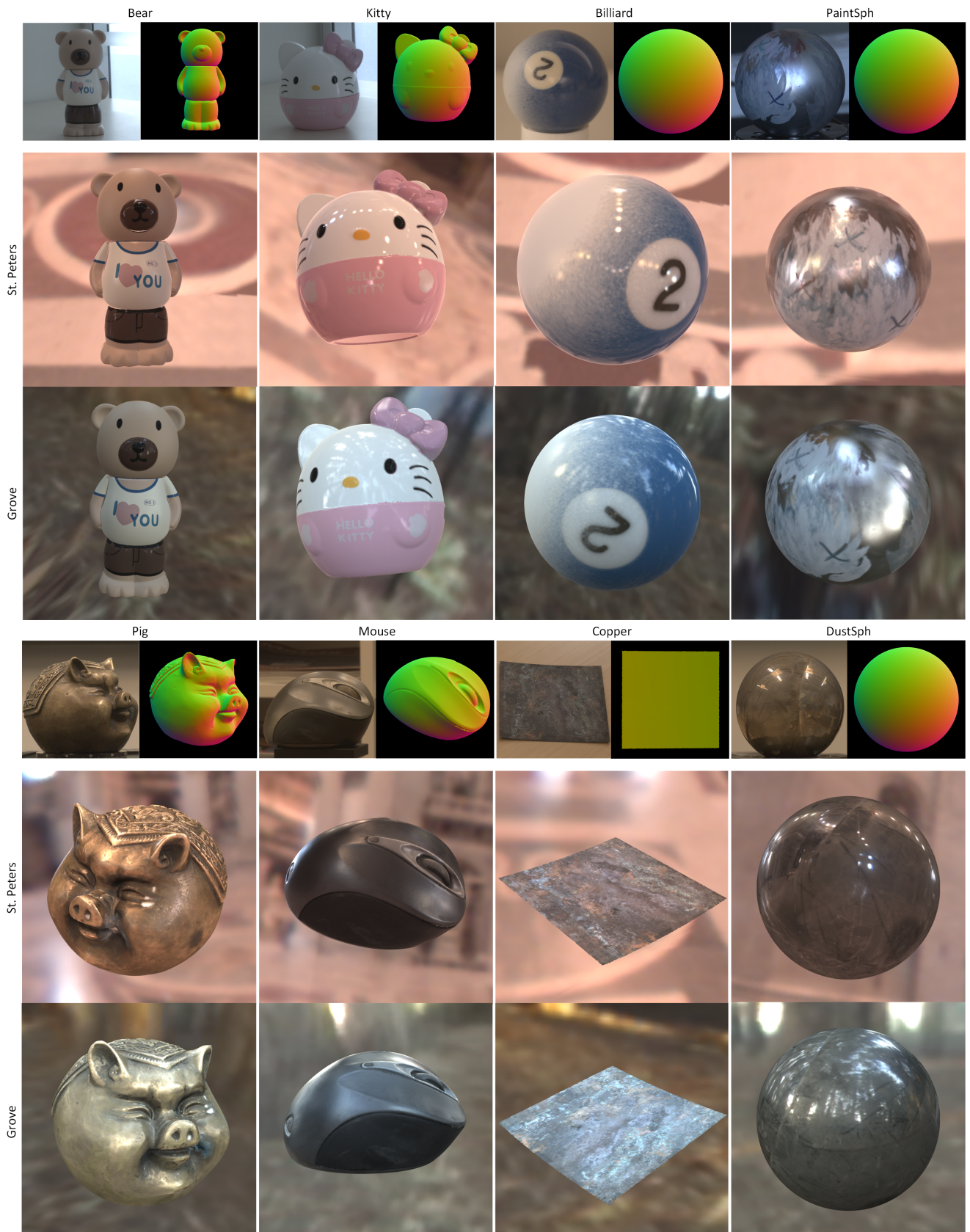


Figure 16: Additional results. Renderings under two novel EMs (St. Peters and Grove) are shown, along with a single captured frame and the acquired geometry in the top row.